

Design and Fabrication of a Soft Magnetic Tactile Sensor

Mahdis Rabbani
School of Mechanical Engineering
University of Tehran
Tehran, Iran
rabbani.mahdis@ut.ac.ir

Mohammad Amin Mirzaee
School of Mechanical Engineering
University of Tehran
Tehran, Iran
amin.mirzaee@ut.ac.ir

Mahdi Robati
School of Mechanical Engineering
University of Tehran
Tehran, Iran
mahdi.robati@ut.ac.ir

Ali Sadighi
School of Mechanical Engineering
University of Tehran
Tehran, Iran
asadighi@ut.ac.ir

Abstract— Tactile sensing has always been a challenging area for robotic systems. Tactile sensors are required to provide necessary feedback on the contact surface between the robot and the target object to ease the manipulation and mimic the human touch. This paper covers a soft magnetic tactile sensor's design, calibration, and validation process. Employing the modeling techniques proposed in this study, one can easily adjust the mechanical characteristics of the sensor to meet the required specifications. A custom test rig is designed and built to apply known forces accurately and log the sensor's output to perform the calibration process. Moreover, the sensor's specifications and errors under high and low force slopes have been examined and reported. Finally, the sensor's transfer function has been estimated using its step response.

Keywords— force sensor, soft tactile sensor, magnetic sensor, Multi-layer Perceptron, Neural Networks

I. INTRODUCTION

Tactile sensing remains state-of-the-art in robots interacting with the surrounding environment. Tactile sensors are devices that discern surface properties when they come into physical contact with objects [1], [2]. They can quickly adapt to their surroundings due to their flexibility and softness. Tactile sensing in legged robots enables the robot to walk on rough terrain [3], [4]. When integrated into manipulators and robotic arms, Tactile sensors can facilitate grasping various objects [5]. A critical application of tactile sensors is slip detection in robotic hands while holding objects [6]. They are also widely used in medical applications and surgical robots [7], [8].

Various transduction mechanisms can be employed in the design of tactile sensors. Schmitz et al. [9] proposed a tactile sensor that converted mechanical parameters into signals using capacitive pressure sensors. The soft dielectric between the sensor's two electrodes deformed under load, causing the capacitance to change. Lin et al. [10] developed a novel flexible piezoelectric tactile sensor inspired by human skin. Wang et al. [6] created a flexible tactile sensor array to detect the distribution of applied external force based on resistance changes between flexible layers. Vision-based tactile sensors capture the deformation of a pattern on the contact surface of the sensor [11], [12]. Tracking this pattern results in information such as the applied force and object shape. The sensor technologies mentioned above each have their own pros and cons. However, almost all of them are relatively costly and difficult to integrate into robotic arms.

Tactile sensors based on magnetic fields have shown the potential to reach high performance at an affordable cost [13]. The concept of using magnets in tactile sensors was firstly proposed in 1988 [14]. However, magnetic field sensing technology was limited at that time. With the advancement of technology, this group of tactile sensors has become one of the most affordable sensors to be used in robotic applications. These sensors can be designed and fabricated in different sizes. Chatzipirpiridis et al. [16] proposed the most miniature magnetic force sensor with a maximum dimension of 2 mm that can be used in medical applications. A soft tri-axis tactile sensor was developed and tested [15]. This sensor measured the magnetic field variation of a permanent magnet embedded in a deformable elastomer. Other sensors based on the same principle are introduced that use different mechanical designs [17], [18].

None of the reviewed papers, whether magnetic or not, reported the effect of the rate of applied forces on the sensor precision and response. As the deformable compliance is made of soft elastomer, it mostly shows viscoelastic and hyperelastic behavior [19]. This effect makes the sensor respond differently when subjected to different force slopes, as it has a stress integrator term in the strain formula. That being said, the final force value might alter by changing the force slope. Moreover, the design procedure of the sensors above does not present a reliable approach to predicting and adjusting the sensor's specifications before fabrication.

In this paper, a soft magnetic tactile sensor is designed and studied. With the technique presented in this study, the mechanical properties of the sensor can be easily modified to meet desired specifications. As all the mechanical components are 3D-printed, they can be redesigned at a much lower cost. Also, the sensor's performance under various force slopes is investigated in this paper. The steps and constraints for designing the sensor are discussed in section II. The instrumentation required to test the sensor is designed in section III, and electrical and software components are introduced. Section IV contains the neural network algorithm employed to calibrate the sensor. The neural network is implemented on the microcontroller in section V, and the sensor's transfer function is estimated.

II. SENSOR DESIGN

The proposed sensor design comprises two main subsystems, as shown in Fig. 1. The primary subsystem

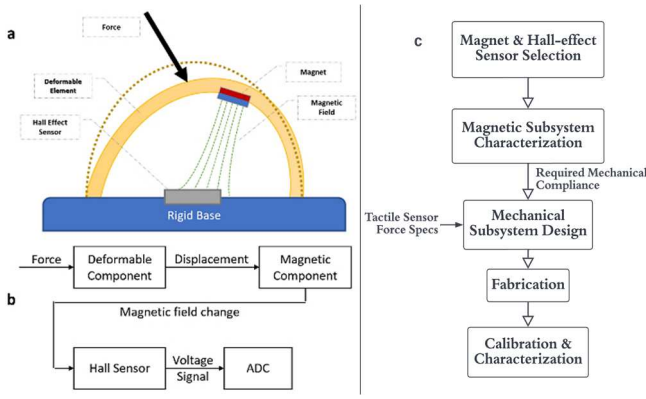


Fig. 1. (a) Sensor design and working mechanism of the sensor. (b) Measurement chain of the proposed sensor, (c) Development process of the tactile sensor.

consists of a deformable component with a magnet underneath that deforms noticeably in response to load. This deformation affects the magnet's orientation and position within the magnetic subsystem, which changes the spatial distribution of the magnetic field. A Hall-effect sensor is then employed, which outputs an electrical signal proportional to the magnetic field variation from which applied force can be inferred.

The design process begins with selecting the magnetic subsystems' elements, i.e., magnet and Hall-effect sensor. Then, it is required to study the effect of the magnet displacement on the magnetic field seen by the Hall-effect sensor. This study is done analytically, followed by experimental validation. The appropriate compliance for the mechanical subsystem is determined by combining the desirable displacement range found in this stage with the tactile sensor's demanded force specifications. The mechanical subsystem design is then pursued to achieve the specified compliance. The development process for the tactile sensor is shown in Fig. 1 (c).

A. Magnetic Subsystem

An N35 cylindrical (3x1 mm) magnet along with a three-axis Hall-effect sensor (AK8963) are used in the current design. The magnet relative motion with respect to the Hall-effect sensor must yield maximum sensitivity without saturating the sensor, which occurs at 4.8 mT for AK8963.

Calculating the magnet's magnetic flux density is necessary to determine the smallest distance from the sensor that can be maintained without saturation. The relationship between magnetic flux density and distance from the magnet surface is given by [20]:

$$B = \frac{B_r}{2} \left(\frac{D+z}{\sqrt{R^2+(D+z)^2}} - \frac{z}{\sqrt{R^2+z^2}} \right) \quad (1)$$

Where D is the cylinder's height, z is its distance from the magnet's upper surface, R is its radius, and B_r is the magnet's residual magnetism or remanence field. In this study, D , R , and B_r are set to 1 mm, 1.5 mm, and 1.17 T, respectively.

The equation (1) has been solved for the distance z , considering the magnetic flux density B is set to 4.8 mT. The corresponding z is obtained 6 mm. So, to avoid saturation, this distance must be monitored. Nevertheless, this distance is determined using the theoretical equation provided by (1). Since a magnet's properties can change due to demagnetization, this critical distance might be different in the

experiment. Thus, an experiment has been conducted to measure the magnetic flux density of the magnet on its axis at different distances set by a micropositioning stage, shown in Fig. 2.

The experimental results, along with the curve obtained from (1), are shown in Fig. 3. It is observed that both curves are very close for large and considerable distances. However, according to the experimental result, the saturation occurs just below 6 mm. So, keeping a distance of 6.4 mm provides a safe margin. Also, to maximize the sensor sensitivity, the steepest interval of the curve is chosen for the normal operating range, as shown in Fig. 3.

B. Mechanical Subsystem

The mechanical subsystem consists of a hemispherical shell that deforms when subjected to an external force. This specific geometry allows for considerable deformation under various loading orientations.

Shell's material, radius, and thickness are substantial in determining its compliance. Given the force specification of the tactile sensor (5 N) and the desirable displacement range (1.6 mm), the required compliance is about 0.32 mm/N. Since the flexible resin used in this study as the compliant material shows viscoelastic properties, extracting the material's mechanical properties and mechanical analysis of the dome is challenging. Thus, to determine the stress-strain curve, a unidirectional tensile test is performed, and Abaqus Finite Element Analysis software is used for the mechanical analysis of the dome.

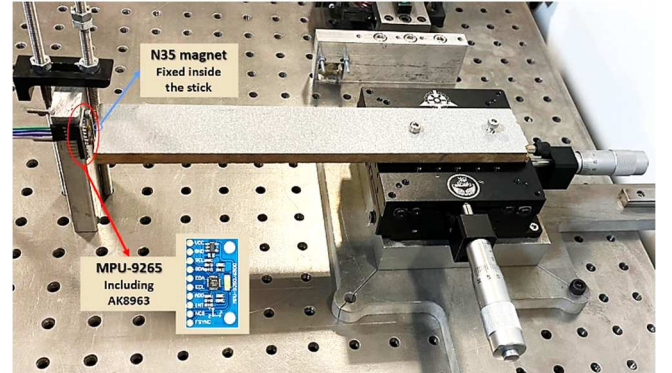


Fig. 2. Verifying the experimental data with theoretical results. A micropositioning stage is used to place the N35 cylindrical magnet at specific distances from AK8963.

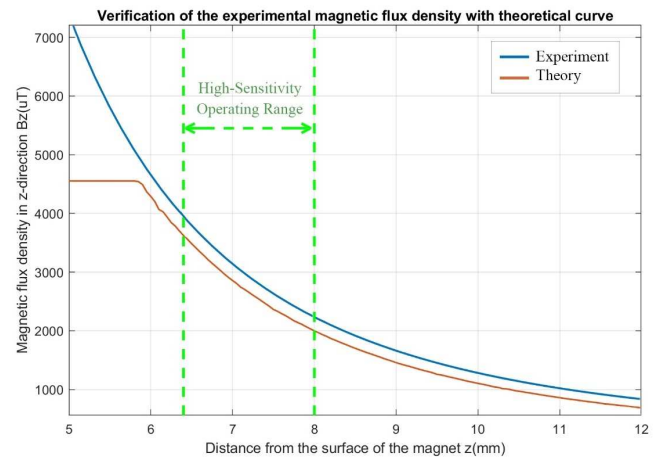


Fig. 3. Distance – magnetic flux density relationship.

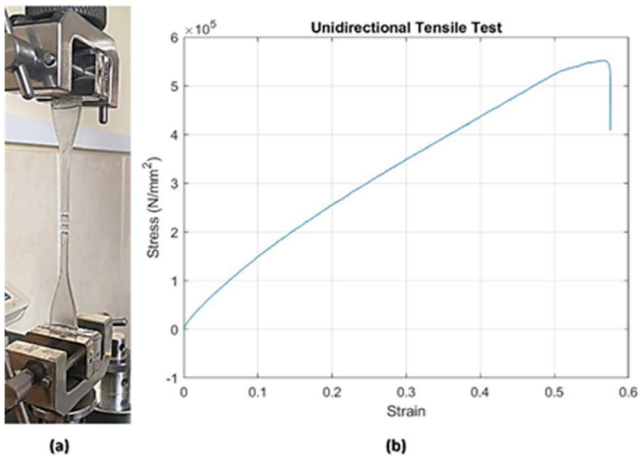


Fig. 4. (a) Tensile test conducted on the dog bone specimen made of 3D-printed resin, (b) Result of the tensile test on the flexible 3D-printed resin. The specimen is an ASTM D638 standard-based type IV dog bone with a width of 4 mm and tensile rate of 10 mm/min.

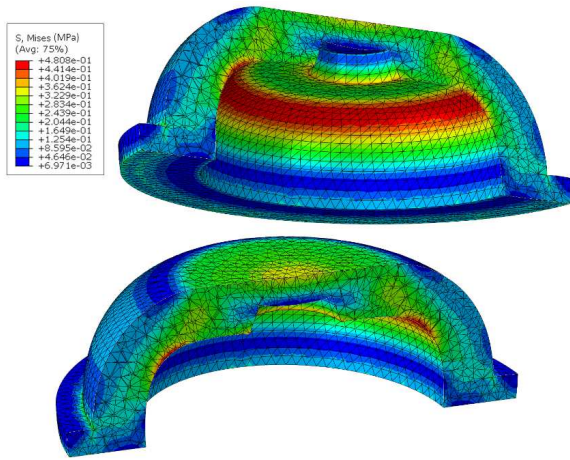


Fig. 5. Mechanical analysis of the dome in Abaqus.

The tensile test's resulting curve, shown in Fig. 4, is fed to Abaqus software to analyze the behavior of the dome under different loadings. Among all hyperelastic models, Mooney-Rivlin best fits the data with parameters c_{10} and c_{01} of 0.1182 MPa and 0.1769 MPa, respectively. The mesh elements are quadratic Tets with a hybrid formulation. The contact type between the dome and the rigid body is set to be hard contact with a friction coefficient of 0.8.

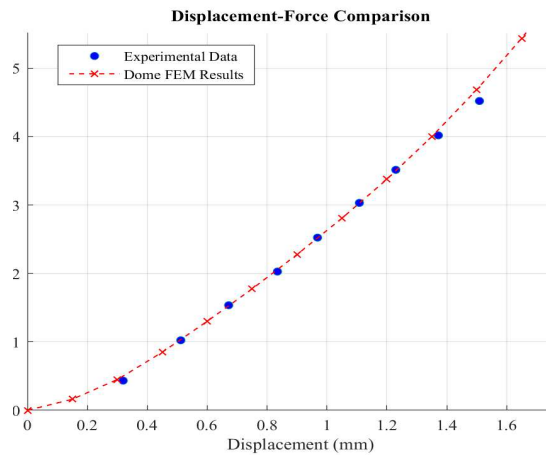


Fig. 6. Force-displacement curve comparison between experimental data and FEM simulation.

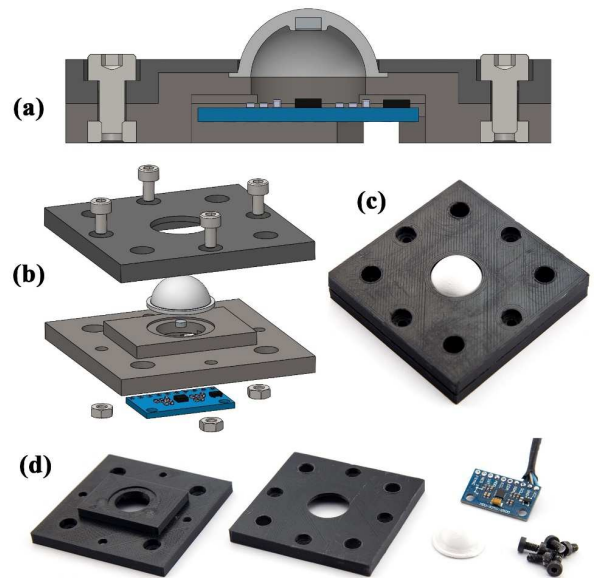


Fig. 7. (a) CAD cross-section of the sensor, (b) Exploded view of the CAD sensor, (c) Assembled prototyped sensor with 3D-printed parts, (d) 3D-printed parts and Hall-effect sensor.

After a couple of trials, it is observed that a dome made of resin with an outer radius of 8 mm and thickness of 2 mm will have the required compliance. Fig. 5 shows the stress contour of the FE analysis. According to these results, the maximum stress of the designed dome subjected to the maximum applied force is much lower than the tensile strength of the deformable resin.

Fig. 6 illustrates the force-displacement curve predicted by simulation and the experimental test. Each experimental data was obtained by calculating the steady-state response of the sensor to a step input. It is observed that the FEM and experimental results are close, and FEM is verified. Thus, one can perform simulations to achieve the desired specifications before fabrication. Fig. 7 (a) shows the assembled sensor's cross-section and exploded view. The sensor body and the compliance were made by 3D-printing PLA and deformable resin, respectively.

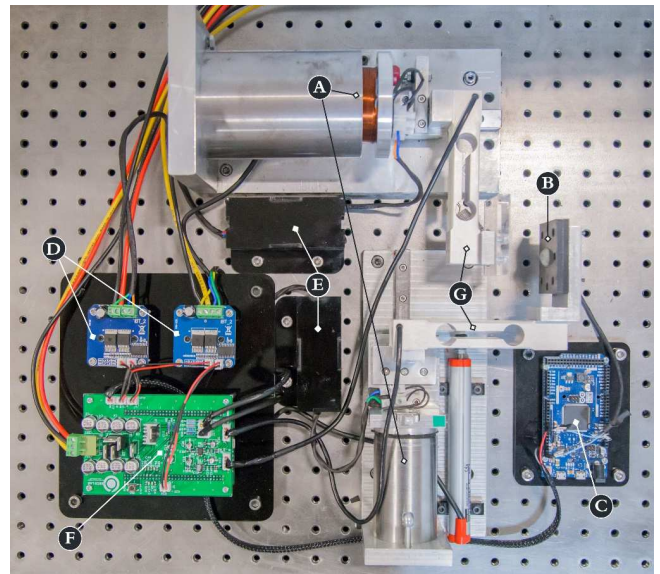


Fig. 8. Test rig. (A) Voice coil actuators, (B) Proposed tactile sensor, (C) Arduino Due, (D) Drivers, (E) Filters, (F) Force measurement, (G) Load cells.

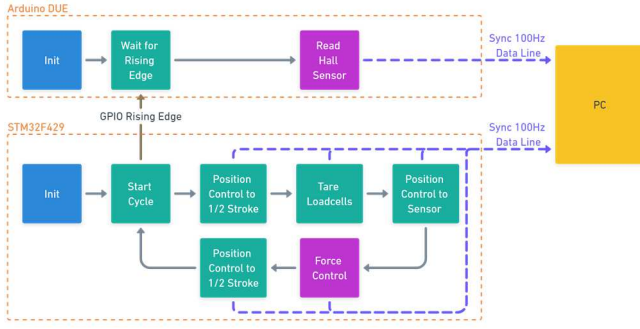


Fig. 9. Working flowchart of the STM32 and Arduino Due.

III. TEST RIG DESIGN

The relationship between the applied force and sensor output must be known for the sensor to work correctly. According to the measurement chain shown in Fig. 1 (b), one way to find such a relationship is to use theoretical governing equations of two subsystems. However, modeling errors will lead to low accuracy of the tactile sensor. Instead, a nonlinear mapping, in the form of neural networks, is established between the sensor input and output.

The approach includes feeding the measured magnetic flux density to the network and predicting the applied force. This approach is known as the inverse modeling technique [21]. In this strategy, the sensor output is recorded for known applied forces. To enable an accurate force application and record the sensor output, a custom test rig was developed, as shown in Fig. 8. It consists of primary and secondary stages, which are used to apply axial and lateral forces in an accurately controlled way.

Two load cells are used in both stages to measure the applied force to the deformable dome. The load cell is made of four strain gauges in a Wheatstone bridge, requiring instrumentation to filter the noise, differentiate the load cell output signals, and amplify the differentiated signal. Here, a capacitance multiplier was used for supply noise rejection, and an AD620 instrumentation amplifier was used to differentiate and amplify the load cell output signals. The final signal was sampled using a 12-bit analog-to-digital converter of the STM32F429I-DISC1 microcontroller.

The voice coil actuators [22], including motor drivers and the microcontroller that make up the force control part, use the measured force as feedback and calculate the control effort based on the calculated error. The BTS7960 motor driver receives the control effort as a PWM signal. The PWM operates at the BTS7960 module's maximum allowable frequency of 25 kHz. A low-pass filter is used to attenuate this high-frequency component in order to have a clean actuator force. The tactile sensor is attached to the secondary stage load cell, and its output voltage is sampled at a 100 Hz rate and transferred to Arduino Due via an I²C communication protocol.

Data acquisition should begin and end simultaneously on two microcontrollers. Fig. 9 depicts the microcontrollers' operational flowchart. As soon as STM32F429 begins sampling a single data, Arduino Due is triggered by a hardware interrupt. Then, the synchronized data is sent to the computer using a USB connection.

As illustrated in Fig. 9, voice coil actuators are position controlled to the half-stroke in the first step so that no forces

are applied to the load cells. The load cells are then tared to show zero force in the software. The normal load cell then moves gradually in the direction of the sensor to minimize the impact before the force control mode is activated. Finally, the voice coils return to half-stroke, and the system is restarted.

IV. CALIBRATION

The calibration process is necessary for all sensors. It is mainly done to reduce the systematic error of measurement and to improve the sensor's accuracy.

The sensor has been calibrated using the represented force control mechanism. The tangential axis was fixed during the data acquisition to calibrate the sensor's normal force. With the viscoelasticity of the compliance material, the loading rate affects the Hall-effect sensors' signals, resulting in different values under the same applied force. Therefore, the loading rate plays a fundamental role for the sensor.

According to this effect, data was collected while various sloped ramp forces were applied to the sensor. The slope range was from 0.025 N/s to 0.7 N/s, with the final maximum force of 5 N. The slopes are shown in TABLE I. Nine out of the eleven datasets were used to train the model and two for the test, one steep and one moderate slope.

As the linear regression algorithm could not map the three Hall-effect sensor signals to the normal force, Multi-Layer Perceptron (MLP) models were utilized for the regression analysis of the sensor. MLPs can be optimized to identify the nonlinearity of the systems.

The MLP models were constructed on the open-sourced Python 3.7 and Tensorflow 2.0 platform. This algorithm is based on the back-propagation learning method. As shown in Fig. 10, inputs are multiplied by the first layer's weights and summed by the biases. Then activation function is applied to the calculated value. The same is performed for all hidden layers to the output layer.

The MLP model has multiple hyperparameters that can be tuned to construct the optimal architecture of the MLP model. Some of these hyperparameters (learning rate and epoch) were fixed in the first step of this study. The number of hidden layers and the neurons, activation functions, batch size, and other hyperparameters were selected from a list of options.

Moreover, the input scaling can significantly affect the performance. Regarding this, MinMax and StandardScaling were both tested on the models. Ultimately, a grid search,

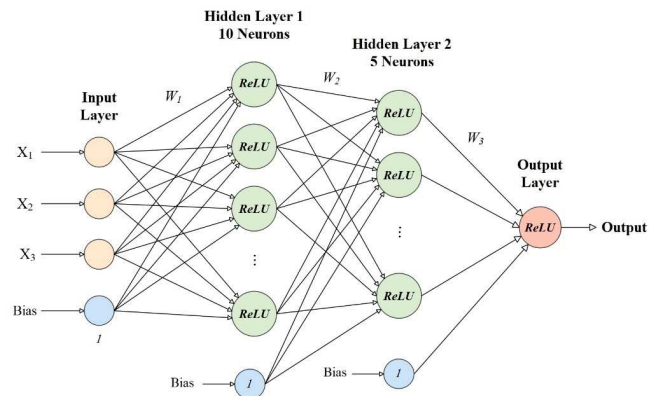


Fig. 10. Optimal Multi-Layer Perceptron architecture. The optimal model has two hidden layers added to the input and output layers with a 3-10-5-1 structure.

TABLE I. DATA DIVISION

All Slopes (N/s)	Train					Test
	0.1	0.2	0.3	0.4	0.6	0.5
	0.7	0.8	0.025	0.075		0.05

TABLE II. OPTIMAL MODEL ARCHITECTURE

Model Layer Structure	3-10-5-1	Optimizer	ADAM
Activation Functions	ReLU	Learning Rate	0.001
Scaling Method	MinMax	Batch Size	64
Loss Function	MAE	Epoch	100

comprised of 400 models, was performed on these parameters to find the optimal architecture of the model for the sensor data. The optimal model was selected based on the Mean Squared Error and regression coefficient on all data points. In the next step, the optimal model was retrained with a much lower learning rate for greater epoch numbers.

The architecture of the optimal model is presented in TABLE II. This model consists of a 3-10-5-1 architecture (three input parameters, two hidden layers of ten and five perceptrons, and a single output). The model has a Mean Absolute Error of 0.175 for the train data and 0.201 for the test data. The target values were not scaled in this study as it generally does not affect the model's performance.

The weights and biases of the optimal model were transferred to Arduino Due in the array format. The three signals of the Hall-effect sensor are fed to the implemented model, and the normal force is estimated.

V. TEST AND RESULTS

Fig. 11 shows the model's performance on two ramp forces of different slopes. It can be inferred that steeper loading rates result in higher force estimation errors. The results of the less steep rates show an underprediction of the model at high force values, in contrast to the steep data, which mostly overpredicts the force value in the top half forces. Both datasets' predictions mostly lay in the 10 percent interval error of the actual force, except for the steep data around 1 N, which is highly drifted from actual values.

The cumulative data fraction of the model's predictions for the two datasets is illustrated in Fig. 12. As the moderate slope data curve implies, more than 95 percent of the prediction points deviate less than 10 percent relative to the actual force values. However, the steep data has a relative deviation of more than 25 percent for the same fraction of data points. At the deviation of 38 percent, all the points of the steep force are covered. However, as discussed earlier, most of the error of this dataset (steep) is due to the scattered force predictions around 1 N, which causes the data points to be covered at a much higher relative deviation value. By calculating the maximum absolute error for the two datasets, it is observed that the model has a maximum absolute error of 0.223 N on the steep force and 0.247 N on that of the moderate slope. Moreover, the former slope shows a much smoother estimation compared to the latter.

According to mentioned comparisons, the sensor showed better prediction performances when the load changed at a slower pace. To better characterize the designed sensor and its errors, a step loading with a step size of 3 N and a step time of

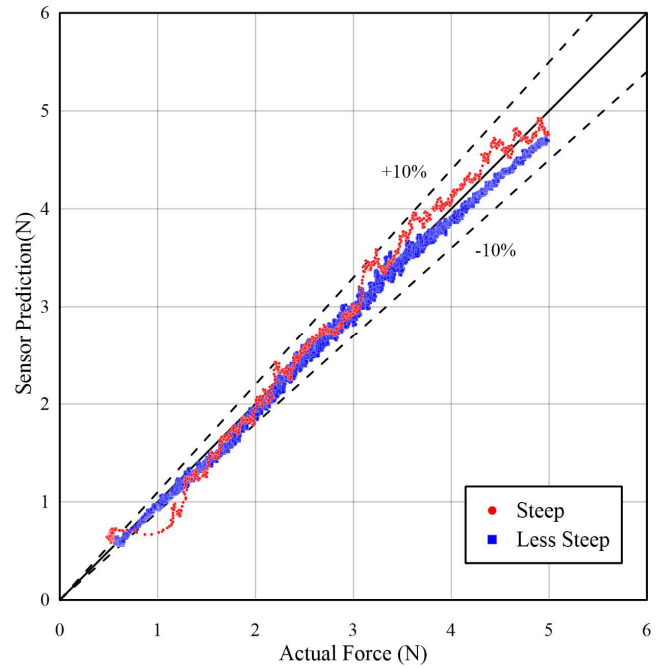


Fig. 11. Prediction result of the optimal model. The x-axis data is obtained from the load cell, while the y-axis is the output of the MLP model running on Arduino Due.

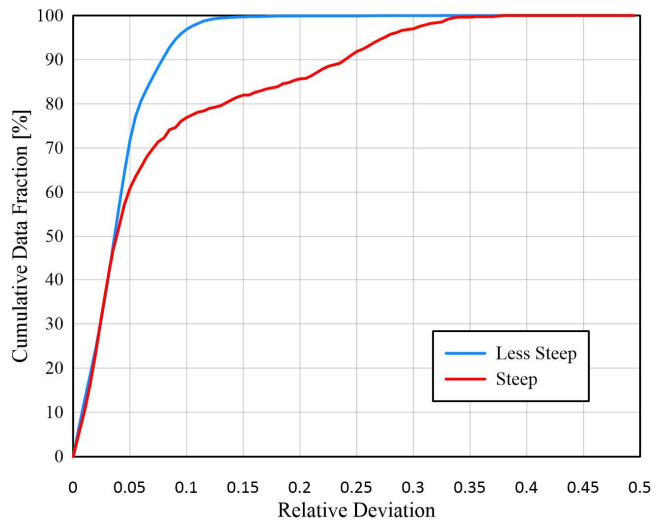


Fig. 12. Cumulative data fraction of the two test datasets. The Sensors deviation is relatively low for slow changes, while it gets higher as the force slope increases.

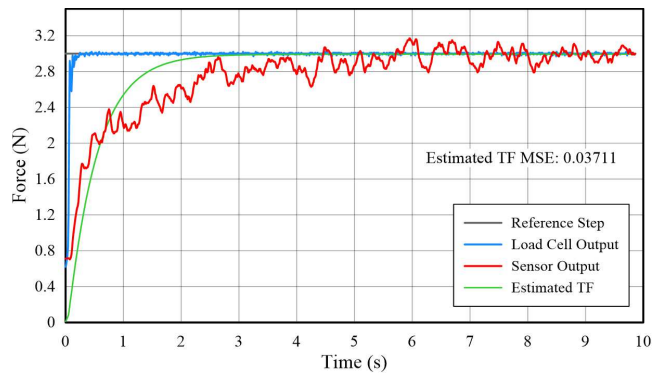


Fig. 13. Step response of the sensor along with the estimated transfer function (TF).

10 s was applied to the sensor. The result is represented in Fig. 13. As the mechanical system of the force mechanism has its own dynamics, it takes some time for the 3 N force to be applied to the sensor. The curves indicate that the calibrated sensor has a rise time of approx. 2.5 s with a variance of 0.172. The response is similar to that of a system with a large damping ratio, corresponding to the mechanical properties of the compliance (as it is made of deformable resin).

To identify the sensor's dynamics and improve its performance, its discrete transfer function was estimated. The step response of the estimated transfer function is compared to the sensor's actual output in Fig. 13. It can be observed that the estimated transfer function consists of a pole close to 1 and a zero on the origin, as given by:

$$G(s) = \frac{0.01955}{1-0.9804 z^{-1}} \quad (2)$$

VI. CONCLUSION

Modeling, design, prototyping, testing, and validation of a soft magnetic tactile sensor have been investigated in this paper. The mechanical part of the sensor was 3D-printed. Before printing, the compliance was simulated in FEM software to estimate its characteristics and finalize the design. Also, some tests were conducted on the material to obtain its mechanical properties correctly. Then, the dome was 3D-printed, and the sensor was assembled. The final results of the prototyped sensor are consistent with that of the simulations. In fact, the soft compliance can be easily modified to reach a suitable design that satisfies the desired specifications, such as force range and sensitivity. By collecting data using the force control system, the normal force of the sensor has been calibrated and validated. It has been observed that the sensor shows better performance on the moderate-slope force, which correlates with the result of the step response that indicates a high damping ratio and settling time. In the end, the calibrated sensor has a maximum operating force of 5 N, with a maximum relative deviation of 10 to 35 percent that varies as the force slope changes. The system's estimated discrete transfer function has a pole close to 1 on the real axis and a zero on the origin. For future studies, the tangential and normal forces can be applied simultaneously to the sensor. Also, a digital compensator can be designed to improve the step response of the sensor.

ACKNOWLEDGMENT

The authors would like to acknowledge the help provided by Mr. Hamidreza Akef for his contributions and efforts.

REFERENCES

- [1] R. S. Dahiya, G. Metta, M. Valle and G. Sandini, "Tactile Sensing—From Humans to Humanoids," in *IEEE Transactions on Robotics*, vol. 26, no. 1, pp. 1-20, Feb. 2010, doi: 10.1109/TRO.2009.2033627.
- [2] Yousef, Hanna, Mehdi Boukallel, and Kaspar Althoefer. "Tactile sensing for dexterous in-hand manipulation in robotics—A review." *Sensors and Actuators A: physical* 167.2 (2011): 171-187.
- [3] G. Zhang, Y. Du, Y. Zhang and M. Y. Wang, "A Tactile Sensing Foot for Single Robot Leg Stabilization," 2021 IEEE International Conference on Robotics and Automation (ICRA), 2021, pp. 14076-14082, doi: 10.1109/ICRA48506.2021.9560967.
- [4] Luneckas, Mindaugas, et al. "A hybrid tactile sensor-based obstacle overcoming method for hexapod walking robots." *Intelligent Service Robotics* 14.1 (2021): 9-24.
- [5] L. Massari, C. M. Oddo, E. Sinibaldi, R. Detry, J. Bowkett, and K. C. Carpenter, "Tactile sensing and control of robotic manipulator integrating fiber Bragg grating strain-sensor," *Front Neurorobot*, vol. 13, Apr. 2019, doi: 10.3389/fnbot.2019.00008.
- [6] Y. Wang, X. Wu, D. Mei, L. Zhu, and J. Chen, "Flexible tactile sensor array for distributed tactile sensing and slip detection in robotic hand grasping," *Sens Actuators A Phys*, vol. 297, Oct. 2019, doi: 10.1016/j.sna.2019.07.036.
- [7] T. Ohtsuka, A. Furuse, T. Kohno, J. Nakajima, K. Yagyu, and S. Omata, "Application of a New Tactile Sensor to Thoracoscopic Surgery: Experimental and Clinical Study," 1995.
- [8] Bandari, Naghme, Javad Dargahi, and Muthukumaran Packirisamy. "Tactile sensors for minimally invasive surgery: A review of the state-of-the-art, applications, and perspectives." *Ieee Access* 8 (2019): 7682-7708.
- [9] A. Schmitz, P. Maiolino, M. Maggiali, L. Natale, G. Cannata, and G. Metta, "Methods and technologies for the implementation of large-scale robot tactile sensors," *IEEE Transactions on Robotics*, vol. 27, no. 3, pp. 389-400, Jun. 2011, doi: 10.1109/TRO.2011.2132930.
- [10] W. Lin, B. Wang, G. Peng, Y. Shan, H. Hu, and Z. Yang, "Skin-Inspired Piezoelectric Tactile Sensor Array with Crosstalk-Free Row+Column Electrodes for Spatiotemporally Distinguishing Diverse Stimuli," *Advanced Science*, vol. 8, no. 3, Feb. 2021, doi: 10.1002/advs.202002817.
- [11] Donlon, Elliott, et al. "Gelslim: A high-resolution, compact, robust, and calibrated tactile-sensing finger." 2018 IEEE/RSJ International Conference on Intelligent Robots and Systems (IROS). IEEE, 2018.
- [12] James, Jasper Wollaston, Nicholas Pestell, and Nathan F. Lepora. "Slip detection with a biomimetic tactile sensor." *IEEE Robotics and Automation Letters* 3.4 (2018): 3340-3346.
- [13] Ledermann, Christoph, et al. "Tactile Sensor on a Magnetic Basis using novel 3D Hall sensor-First prototypes and results." 2013 IEEE 17th International Conference on Intelligent Engineering Systems (INES). IEEE, 2013.
- [14] Clark, James J. "A magnetic field based compliance matching sensor for high resolution, high compliance tactile sensing." *Proceedings. 1988 IEEE International Conference on Robotics and Automation. IEEE*, 1988.
- [15] Wang, Hongbo, et al. "Design methodology for magnetic field-based soft tri-axis tactile sensors." *Sensors* 16.9 (2016): 1356.
- [16] Chatzipirpiridis, George, et al. "Miniaturized magnetic force sensor on a catheter tip." 2015 Transducers-2015 18th International Conference on Solid-State Sensors, Actuators and Microsystems (TRANSDUCERS). IEEE, 2015.
- [17] Chaturanga, Damith Suresh, et al. "Magnetic and mechanical modeling of a soft three-axis force sensor." *IEEE Sensors Journal* 16.13 (2016): 5298-5307.
- [18] Harber, Evan, et al. "A tunable magnet-based tactile sensor framework." 2020 IEEE SENSORS. IEEE, 2020.
- [19] Yuan, Wenzhen. *Tactile measurement with a gelsight sensor*. Diss. Massachusetts Institute of Technology, 2014.
- [20] Camacho, Juan Manuel, and Victor Sosa. "Alternative method to calculate the magnetic field of permanent magnets with azimuthal symmetry." *Revista mexicana de física E* 59.1 (2013): 8-17.
- [21] S. A. Khan, D. T. Shahani, and A. K. Agarwala, "Sensor calibration and compensation using artificial neural network," 2003.
- [22] Saeedi, Suorena, Ali Sadighi, and Masoud Shariat Panahi. "Development of an Optimally Designed Voice-Coil Actuator." 2021 9th RSI International Conference on Robotics and Mechatronics (ICRoM). IEEE, 2021.